Silver Nanoplate Contrast Agents for *In Vivo* Molecular Photoacoustic Imaging

Kimberly A. Homan, **Michael Souza**, **Ryan Truby**, **Geoffrey P. Luke**, **Christopher Green**, **Erika Vreeland**[ŧ], and **Stanislav Emelianov**[*]
Biomedical Engineering Department, The University of Texas at Austin, 1 University Station C0800, Austin, Texas, 78712, USA

[ŧ]Chemical Engineering Department, University of New Mexico, 1 University of New Mexico, New Mexico, 87131, USA

Abstract

Silver nanoplates are introduced as a new photoacoustic contrast agent that can be easily functionalized for molecular photoacoustic imaging *in vivo*. Methods are described for synthesis, functionalization, and stabilization of silver nanoplates using biocompatible ("green") reagents. Directional antibody conjugation to the nanoplate surface is presented along with proof of molecular sensitivity *in vitro* with pancreatic cancer cells. Cell viability tests show the antibody-conjugated silver nanoplates to be nontoxic at concentrations up to 1 mg/ml. Furthermore, the silver nanoplates' potential for *in vivo* application as a molecularly sensitive photoacoustic contrast agent is demonstrated using an orthotopic mouse model of pancreatic cancer. Results of these studies suggest that the synthesized silver nanoplates are well suited for a host of biomedical imaging and sensing applications.

Keywords

contrast agents; photoacoustic imaging; optoacoustic imaging; silver; nanoplates; pancreatic cancer

Molecular imaging of cancer is an area of intense research. Many biomedical imaging techniques are traditionally anatomical in nature but can be adapted, mostly through use of targeted contrast agents, to detect cellular and molecular behavior.[1] One such technique is photoacoustic (PA) imaging.[2] PA imaging is highly complimentary to traditional ultrasound (US) imaging. In US imaging, sound is used to interrogate the body, and an image is reconstructed from sound waves that are backscattered from the tissue's mechanical inhomogeneities. In PA imaging, pulsed laser light is used to interrogate the body, and an image is reconstructed from broadband sound waves generated by light absorption events in various tissue components. US and PA modalities can use the same electronic components for receiving ultrasonic waves, allowing data to be collected from both modalities in a spatially co-registered way. As a result, complementary information about the tissue is obtained: US imaging can visualize anatomy, while PA imaging can visualize functional properties of the tissue based on optical absorption.[3–5]

[*]Corresponding author: emelian@mail.utexas.edu.

SUPPORTING INFORMATION AVAILABLE: Additional figures and supporting video. This material is available free of charge *via* the internet at http://pubs.acs.org.

Contrast in PA imaging arises from the natural variation in the optical absorption of tissue components. Tissue components that absorb light strongly include hemoglobin, fat, and melanin.[6] Of these endogenous components, the use of contrast in PA imaging coming from hemoglobin in blood has been the most widely researched and demonstrated.[7–12] For example, PA imaging can be used to determine the blood oxygen saturation in regions of particular interest, such as cancer, where hypoxia has been shown to be strongly associated with malignancy.[13] Combining US and PA imaging can reveal changes in blood vessel count or oxygen saturation inside tumors as compared with surrounding healthy tissue since anatomical references, such as tumor location, size and boundaries, can be visualized and segmented using US imaging.

The use of endogenous contrast in PA imaging of cancer has made it a popular technique in recent years.[14] However, employing exogenous contrast in PA imaging enables its molecular sensitivity and greatly expands the functionality of the modality.[15–21] Exogenous contrast agents designed for PA imaging usually consist of highly absorbing dyes or nanoparticles that can be conjugated to a targeting moiety of interest.[22–23] The targeting moiety could be an antibody, aptamer, or ligand that will facilitate localization to cancer cells and highlight their presence amongst healthy tissue. Design considerations and requirements for a PA contrast agent include: (1) ease of synthesis with biocompatible reagents, (2) an overall size on the nano-scale or smaller in order to navigate the blood stream and interact with biological macromolecules, (3) a large absorption cross-section of light in the near-infrared (NIR) wavelength region where light penetration into tissue is maximized, (4) a surface chemistry that allows for simple bioconjugation of targeting moieties, (5) low toxicity, (6) long shelf life, and (7) structural and molecular biostability in biological fluids.

Several groups have shown that functionalized gold nanoparticles fulfill most of these requirements and can be successfully employed as PA imaging contrast agents.[17, 24–28] Here, we introduce the use of Ag nanoplates as a new PA contrast agent that meets all of the requirements. The steps of the inherently "green" synthesis methods (*i.e.*, a synthesis using only biocompatible reagents) are described along with the process of functionalizing the nanoplate surface to make it both biostable (structurally stable in physiological media) and antibody-conjugated. The molecular specificity of the nanoplates is demonstrated *in vitro* using pancreatic cancer cell lines and darkfield microscopy. The cytotoxicity of the nanoplates is assessed using two pancreatic cancer cell lines and one non-cancerous pancreatic cell line. Furthermore, the potential of using silver nanoplates for *in vivo* applications is demonstrated through combined ultrasound and photoacoustic (USPA) imaging of an orthotopic pancreatic tumor in a mouse model following systemic injection of antibody-conjugated Ag nanoplates.

RESULTS AND DISCUSSION

"Green" Synthesis and Characterization of Ag Nanoplates

Researchers have designed numerous methods to synthesize Ag nanoplates. Most are accomplished through seed-mediated growth mechanisms[29–40] that can include reducing agents such as hydrazine[41], increases in temperature[30], or even ingenious light mediated methods.[40, 42] Interestingly, even bacteria have been shown to produce silver nanoplates upon incubation with Ag$^+$ in solution.[43–44] Since we intend to use silver nanoplates in a biological context, we adopted a seed-mediated synthesis method that was particularly "green," where only biocompatible chemicals were employed. For instance, ascorbic acid (vitamin C) was used as the reducing agent, and sodium citrate (a well-known preservative) was used as a stabilizing and capping agent during synthesis. Using "green" reagents helped

to facilitate the formation of less toxic nanoplates and speed their transition to biocompatible contrast agents for *in vivo* applications.

After exploring several different methods of preparing Ag seeds[38, 45], we found that the seeds proposed by Xue *et al.*[39] were most reproducible and provided the twinned plane and stacking fault defects that help enable high-yield Ag nanoplates synthesis.[46] To grow the Ag nanoplates from these seeds, we modified procedures introduced by Zou *et al.*[41] where the plates were synthesized in a stepwise process from 4.2 nm seeds to large (> 200 nm edge length) nanoplates. Figure 1 shows the progression of synthesis from seeds to large nanoplates in four steps. First, the yellow seeds were grown into 25 nm nanoplates (B1) as shown in Fig. 1a. Subsequent growth steps increased the edge length of the nanoplates successively (Figs. 1b–1d, representing samples B2–B4, respectively). The colors of the resulting solutions changed with variation of their optical extinction properties as depicted in Figs. 1e and 1f. Our synthesis method produced nanoplates with edge lengths and longitudinal surface plasmon resonances (LSPR) as shown in Table 1. The advantages of this synthesis technique include: (1) only biocompatible reagents are used, (2) Ag nanoplates can be tuned to absorb light throughout the entire visible to near infrared (NIR) light spectrum, and (3) the Ag nanoplate surface is stabilized with sodium citrate, a molecule that can be easily displaced by amine or thiol functional groups for subsequent bioconjugation steps.

Using Ag nanoplates as a NIR beacon for any type of biological sensor or imaging contrast agent application requires that they are stable in saline solutions. While Ag has excellent optical properties for use as a sensor, its lack of structural stability in salt solutions has largely limited its use in biomedical applications. As shown previously[41], when Ag nanoplates are built, the face of the nanoplate grows along the (111) plane, the lowest possible energy surface. A high resolution transmission electron micrograph (TEM) of a silver nanoplate face (from B4) is shown in Fig. S1a. The electron diffraction pattern from that same nanoplate face is shown in Fig. S1b where the first ring of intense spots can be attributed to the (220) Bragg reflections with a lattice spacing of 1.44 Å. This nanoplate surface is most unstable at the tips, where its electromagnetic field enhancements are greatest.[47] Usually it is the loss of these tips that causes the nanoplates' LSPR peak[48] to blue shift, even during idle suspension in water. Therefore, the synthesis technique we chose for silver nanoplates does not yield nanoplates with perfect tips, but instead allows for rounded, more stable tips as shown in Figs. 1 and S1a to be produced.

Allowing for rounded nanoplate tips was only the first step to solving the stability issue. Even Ag nanoplates with rounded tips will degrade and dissolve in salt solutions without additional passivation. To make nanoplates suitable for a contrast agent application, they must be biostable (*i.e.*, structurally stable in a harsh salt or cell media environment) for a minimum of the time period required to circulate in the bloodstream and interact with diseased cells (for cancer applications this time period could be from several hours to a few days). Therefore, we tested the biostability of the Ag nanoplates in Dulbecco's phosphate buffered saline (DPBS) after conjugation of various amounts of thiol-terminated methoxy-poly(ethylene glycol) (mPEG-SH, 5 kDa) to the nanoplate surface (note that PEG was chosen for its well established potential to passivate nanostructures and limit opsonization[49]). The initial conjugation of mPEG-SH to the nanoplates caused a red shift in the LSPR peak of up to 60 nm in the cases where enough mPEG-SH was used to passivate the entire surface. For the example shown in Fig. 2, a 30-fold excess of mPEG-SH was reacted with Ag nanoplates. The nanoplates were washed with water *via* centrifugation and subsequently resuspended in DPBS at day zero. As shown in this case, with correct passivation (an optimal surface area coverage of PEG), the Ag nanoplates were biostable in salt solutions. Their degradation in DPBS was very slow after passivation such that, even

after 62 days, the shift in LSPR was less than 40 nm, there was no evident change in the width of the LSPR peak over time, and only a 6% decrease in extinction was observed. As a control, we created a sub-optimal coverage of mPEG-SH on Ag nanoplates (surface area coverage of only 50%), and upon suspending in DPBS at day zero, a blue shift of over 250 nm was immediate (see Fig. S2). Note that with no passivation or surface modifications, as-prepared Ag nanoplates will completely dissolve when suspended in DPBS. Therefore, functionalizing the Ag nanoplate surface with mPEG-SH passivated the Ag nanoplates, making them suitable for contrast agent applications.

Molecular Specificity and Cytotoxicity of Ag Nanoplates

Functionalizing the surface of noble metals with molecules containing thiols creates strong, covalent thiolate bonds.[50–51] These thiolate bonds are exploited here to not only create biostabilized nanoplates, but also to bind antibodies to the nanoplate surface *via* directional methods. The epidermal growth factor receptor (EGFR) is commonly overexpressed on the surface of cancer cells and promotes tumor growth and proliferation.[52–54] A monoclonal antibody to EGFR (a-EGFR) was used here as a model to target Ag nanoplates to pancreatic cancer cells. The directional conjugation method we used for binding a-EGFR to nanoplates was previously described by Kumar *et al.*[55] This directional method employs linker molecules that bind the Fc portion of the antibody directly to the Ag surface, leaving the entire variable region free to interact with cells. To confirm that the antibody-conjugated Ag nanoplates would target pancreatic cancer cells, while PEGylated Ag nanoplates would have limited interaction, we mixed both types of nanoplates with pancreatic cancer cells *in vitro* for 4 hr. The resulting cells imaged using darkfield microscopy are shown in Fig. 3. The control cells with no nanoplate incubation are seen as blue in darkfield microscopy (Fig. 3a). The cells that were incubated with PEGylated Ag nanoplates have no significant accumulation of silver (Fig. 3b), but the cells that were incubated with a-EGFR-conjugated nanoplates show significant interaction (Fig. 3c). The accumulation of a-EGFR conjugated nanoplates in cells is due to receptor-mediated endocytosis of the nanoplates, as has been shown extensively with a-EGFR conjugated gold nanoparticles and quantum dots.[52, 56–58] These *in vitro* results demonstrate the ability of a-EGFR conjugated nanoplates to molecularly target pancreatic cancer cells.

Since the a-EGFR conjugated nanoplates were proven to target cancer cells, we decided next to study if these interactions induce any cytotoxicity. Therefore, various amounts of a-EGFR conjugated nanoplates were mixed with three different cell lines *in vitro*: MPanc96 and L3.6pl (pancreatic cancer cell lines that overexpress EGFR), and HPNE (a non-cancerous pancreatic cell line). The viability of the cells was tested after incubation with the a-EGFR conjugated nanoplates for 24 hr using an MTS assay. As shown in Fig. 4, even up to concentrations of 1 mg/ml Ag nanoplates, no statistically significant cytotoxicity was found with any of the three cells lines. These results were surprising since the cytotoxicity of 5 nm to 20 nm Ag nanostructures has been characterized at much lower concentrations (less than 0.4 mg/ml).[59–60] Our results suggest that there is possibly a size- or coating-dependent cytotoxicity of silver that deserves further study as recommended in a recent review.[61]

In Vivo Photoacoustic and Ultrasound Imaging with Ag Nanoplates

All *in vivo* imaging studies were conducted on Nu/Nu transgenic mice with xenograft human pancreatic cancer grown orthotopically. Before injection of nanoplates, volumetric PA and US images of the tumor, consisting of multiple 2-D transverse sections of the tumor, were acquired by translating the mouse through the imaging plane. Then a-EGFR, PEG-passivated Ag nanoplates (~10^{12} nanoplates in 200 μl of PBS with LSPR peak at ~800 nm) were injected into the tail vein. Imaging was performed every hour after injection up to 6 hr post injection. At 4 hr post injection, peak accumulation of nanoplates in the tumor was

observed as determined by monitoring the photoacoustic signal intensity with time post injection. US and combined USPA images are shown in Fig. 5. The tumor is outlined in the ultrasound image as the hypoechoic region inside the dotted white line (Fig. 5a) and appears under the spleen and adjacent to the kidney. PA signals captured in a range of wavelengths (740 nm to 940 nm) were used to spectroscopically resolve the signal from blood in Fig. 5b. Translating the mouse through the 2-D cross-sectional USPA imaging plane allowed for reconstruction of a 3-D image of the orthotopic tumor (Fig. 6). To see further spatial distribution of the contrast agent and blood within the tumor space, a video showing a rotating 3-D view of the imaged tissue was created (Fig. S3). As has been shown with other cancer models, a heterogeneous distribution of nanoparticle accumulation in the tumor was observed.[62–63] Furthermore, histological slices of the tumor stained with silver stain and nuclear fast red (Fig. 7) confirmed the heterogeneous nanoplate distribution seen in USPA imaging. These *in vivo* imaging results indicate that silver nanoplates have the ability to accumulate in the tumor space and provide enhanced contrast of the tumor region using PA signals that are easily differentiated from the endogenous tissue contrast (*e.g.*, blood). Employing molecularly targeted nanoplates in this way can be useful for studying the molecular profile of tumors and monitoring molecular therapeutic approaches in future applications.

CONCLUSIONS

Ag nanoplates were synthesized using only biocompatible, "green" methods that resulted in a clean, non-toxic surface ready for thiol-mediated, directional conjugation of targeting and passivating molecules, such as antibodies and PEG. Once conjugated to a-EGFR, functionalized nanoplates underwent receptor-mediated endocytosis in pancreatic cancer cells that overexpress EGFR, demonstrating their potential for molecular specificity *in vitro*. Furthermore, once properly passivated with PEG, Ag nanoplates remained biostable in salt solutions and cell media for over two months. For the concentrations tested up to 1 mg/ml, Ag nanoplates did not inhibit proliferation of three different pancreatic cell lines, indicating they had low cytotoxicity. Furthermore, spectroscopic PA imaging was able to visualize a-EGFR conjugated nanoplates in a mouse model of orthotopic pancreatic cancer and differentiate the Ag nanoplate PA signal from that of the endogenous blood. Overall, the results of these studies suggest that Ag nanoplates are well suited as PA contrast agents and have the potential for use in a host of biomedical imaging and sensing applications.

METHODS

Chemicals

All chemicals were used without further purification and were at a minimum of ACS grade. Silver nitrate (>99%), trisodium citrate (TSC), sodium periodate, the antibody to Epidermal Growth Factor Receptor (EGFR) clone C225, poly(ethylene glycol) bisphenol A epichlorohydrin M_n = 14 kDa, and Bis (p-sulfonatophenyl) phenylphosphine dihydrate dipotassium salt (BSPP) were purchased from Sigma-Aldrich (St. Louis, MO, USA). ACS grade L(+) ascorbic acid was a product of Acros (Morris Plains, NJ, USA). Dulbecco's phosphate buffered saline (DPBS) came from Mediatech, Inc. (Herndon, VA, USA). The methoxy-poly(ethylene glycol)-thiol (mPEG-SH of 5 kDa) was from Laysan Bio (Arab, AL, USA). All cell culture products, including the MTS assay, were purchased from Invitrogen (Carlsbad, CA, USA) unless otherwise specified. Slide mounting media, Vectashield with DAPI stain, was from Vector Laboratories (Burlingame, CA, USA). The linker hydrazide-polyethylene glycol-dithiol (SPT-014B) was a product of Sensopath (Bozeman, MT, USA).

Ag nanoplate synthesis

Ag nanoplates were formed *via* a seed-mediated growth process. Ag seeds were synthesized *via* procedures previously described by Xue *et al.*[40] Specifically, a 250 ml flask was placed in an ice bath and filled with 95 ml of deionized and ultrafiltered (18.2 MΩ-cm) (DIUF) water. In an Ar environment, 1 ml of 30 mM trisodium citrate (TSC) and 0.5 ml of 20 mM silver nitrate ($AgNO_3$) were added. The mixture was stirred at 500 rpm for 20 min. To reduce the silver ions from $AgNO_3$, 1 ml of ice cold 50 mM sodium borohydride ($NaBH_4$) was added quickly, and the solution immediately turned bright yellow. One more ml of the 50 mM $NaBH_4$ was then added dropwise over the following 15 min. In a separate ice cold vial, a solution of 1 ml of 50 mM $NaBH_4$ was added to 1 ml of 5 mM BSPP. That 2 ml mixture of $NaBH_4$ and BSPP was slowly dropped into the vigorously stirring Ag seed solution over a period of 5 min. The Ag seeds were then stirred at 350 rpm and kept at 0°C for 5 hr. Finally, the flask containing the seeds was transferred to 4°C and allowed to age undisturbed overnight. Note that an argon environment was maintained throughout the entire procedure and the flask was wrapped in foil to minimize light exposure.

The Ag seeds were used to grow Ag nanoplates up to 14 days after synthesis, with the peak efficacy (largest translation to plates) occurring on the day after synthesis. The typical peak resonance wavelength of the seeds as prepared was 395 nm at an optical density (OD) of 1 using a 1 cm path length cuvette. Growing nanoplates of sizes up to 250 nm in diameter involved 4 separate growth steps where the product of one step was used as the starting material for the subsequent step, as modified from that described by Zou *et al.*[41] First, a 20 ml vial was filled with 8.0 ml of DIUF water, 50 μl of 40 mM TSC, 150 μl of 40 mM L +ascorbic acid, and 1.8 ml of the as prepared Ag seeds at an OD of 0.65. The mixture was vigorously stirred at room temperature while 5.05 ml of 584 μM $AgNO_3$ was dripped in *via* syringe pump over 10 min. After the 10 min, the solution turned color from bright yellow to orange, red, and maroon. After the $AgNO_3$ addition was complete, the solution was allowed to stir for an additional 10 min and the light extinction spectrum was taken using a DU Series 600 Spectrophotometer (Beckman Coulter). This first solution was called B1. Second, for the next Ag nanoplate growth step, another 20 ml vial was filled with 4.8 ml of DIUF water, 50 μl of 40 mM TSC, 150 μl of 40 mM L(+) ascorbic acid, and 5 ml of B1. Again, the mixture was vigorously stirred at room temperature while 5.05 ml of 584 μM $AgNO_3$ was dripped in *via* syringe pump over 10 min. After the 10 min, the solution turned color from red to purple to blue to teal-green. After the $AgNO_3$ addition was complete, the solution was allowed to stir for an additional 10 min and the light extinction spectrum was taken. This second solution was called B2. Third, for the next Ag nanoplate growth step, another 20 ml vial was filled with 4.8 ml of DIUF water, 50 μl of 40 mM TSC, 150 μl of 40 mM L(+) ascorbic acid, and 5 ml of B2. Again, the mixture was vigorously stirred at room temperature while 5.05 ml of 584 μM $AgNO_3$ was dripped in *via* syringe pump over 10 min. After the 10 min, the solution turned color from teal to forest green to light forest green with a purple hue. After the $AgNO_3$ addition was complete, the solution was allowed to stir for an additional 10 min and the light extinction spectrum was taken. This third solution was called B3. For the fourth and final growth step, another 20 ml vial was filled with 4.8 ml of DIUF water, 50 μl of 40 mM TSC, 150 μl of 40 mM L+ascorbic acid, and 5 ml of B3. Again, the mixture was vigorously stirred at room temperature while 5.05 ml of 584 μM $AgNO_3$ was dripped in *via* syringe pump over 10 min. After the 10 min, the solution turned color from purple to pastel blue. After the $AgNO_3$ addition was complete, the solution was allowed to stir for an additional 10 min and the light extinction spectrum was taken. This fourth and final solution was called B4. The ImageJ application[64] was used to manually size representative populations of the nanoplate and seed batches. Note that Ag nanoplate batches did contain a subpopulation of silver spheres (~15% by particle number). All nanoplate solutions were analyzed using electron microscopy with both a LEO S5500

scanning transmission electron microscope (STEM) and a JEOL 2010F transmission electron microscope (TEM).

Ag nanoplate antibody and poly(ethylene glycol) conjugation

A directional conjugation of the C225 anti-epidermal growth factor receptor antibody (a-EGFR) from Sigma-Aldrich (product number E2156) to nanoplates was performed. Directional procedures were adapted from those previously described for antibody conjugation to gold nanoparticles by Kumar *et al.*[55] A linker molecule was employed to achieve directionality, meaning that only the Fc region, or nonbinding part of the antibody, attached to the silver. The particular linker we used, a hydrazide-polyethylene glycol-dithiol (Sensopath SPT-014B), covalently bound to the glycosylated portion of the antibody (found in the Fc region) through its hydrazide group, while the dithiol groups bound to silver.

Before directional conjugation of a-EGFR to Ag nanoplates could be achieved, first the linker molecule was attached to the antibody. As previously described[55], the antibody was prepped by changing the buffer to a mono/dibasic sodium phosphate buffer (pH = 7.5) using two wash steps in a 50 kDa molecular weight cut off (MWCO) centrifugal filter from Millipore (centrifuge at 3600 rpm for 15 min at 4°C). The antibody was reconstituted in 1.3 ml of the sodium phosphate buffer and placed in a sterile 2 ml tube. To create an aldehyde group on the glycosylated portion of the antibody, 80 μl of fresh 100 mM $NaIO_4$ was added to the antibody and allowed to shake in the dark for 30 min at room temperature. The reaction was quenched by the addition of 500 μl of 1× phosphate buffered saline. Then, 6 μl of 427.4 mM linker in anhydrous ethanol (kept at −80°C prior to use) was added to the antibody solution and allowed to react for 1 hr while shaking at room temperature. Finally, the antibody-linker (AB-linker) conjugate was cleaned using HEPES buffer in the same 50 kDa MWCO Millipore filters described above and then reconstituted in 300 μl HEPES buffer (pH = 8.0) for storage. The AB-linker conjugate can be stored at 4°C and will remain viable for the life of the antibody. A 75% to 85% yield of the AB-linker conjugate can be expected using this technique if strict and clean pipetting techniques are employed throughout the process.

Once the AB-linker conjugate was built, further conjugation to the Ag nanoplates was facile. Briefly, a B4 batch of nanoplates was placed in a 50 kDa MWCO Millipore centrifugal filter directly after synthesis and spun at 1500 rcf for 5 min at 20°C. The nanoplates were then resuspended in 1 ml of DIUF water and placed in a 2 ml tube. Then, enough of the AB-linker solution was added to account for 0.05 mg of antibody-linker (the exact volume of the AB-linker solution varied based on the final concentration of the AB-linker in HEPES as determined by a Thermo Scientific Nanodrop read at a wavelength of 280 nm with an assumed extinction coefficient of 210,000 $M^{-1}cm^{-1}$). The AB-linker and nanoplates were allowed to shake at room temperature in the dark for 20 min. No shift in peak resonance of the nanoplates was observed after conjugation of the AB-linker to the nanoplates.

To enhance biocompatibility and stability, the surface area of the silver not covered by antibody was passivated by attachment of poly(ethylene glycol) (PEG). Specifically, after allowing the AB-linker and Ag nanoplate solution to shake for 20 min, 50 μl of a 2 wt% PEG (M_n = 14 kDa from Sigma-Aldrich) was added to prevent aggregation and 40 μl of 50 mM mPEG-SH (5 kDa from Laysan Bio) was also added to react with the Ag nanoplates. After shaking in the dark for 20 min, the nanoplates were cleaned using 50 kDa MWCO Millipore centrifugal filters spun at 1500 rcf for 5 min at 4°C. The nanoplates were then resuspended in 500 μl of PBS and sent through a 0.22 μm filter into a sterile 2 ml tube for future use. The antibody-conjugated Ag nanoplates can be stored at 4°C for the life of the antibody. A 40 to 60 nm red shift in the peak resonance of the nanoplates was observed directly after the mPEG-SH passivating step.

Ag nanoplate biostability

Silver in nanoform is known to be a mesostable compound. Passivation of the reactive Ag surface with polymers such as poly(ethylene glycol) (PEG MW = 5 kDa) is required to maintain the shape and optical properties of Ag nanoplates. For instance, if Ag nanoplates are left in growth solution overnight, their peak resonance will blue shift by up to 120 nm by the next day. If Ag nanoplates are cleaned and resuspended in DIUF water, they will blue shift by ~80 nm over the next 20 days. This blue shift in peak resonance is generally due to loss of sharp triangular plate tips since they are the regions of highest surface energy on the plate. Furthermore, without surface passivation, when Ag nanoplates are placed in PBS, they dissolve. For biological applications, it is required that Ag nanoplates remain stable for days in PBS and cell media. Therefore, we tested the stability of Ag nanoplates over time after passivating the surface with mPEG-SH (5 kDa, Laysan Bio).

To test the passivating effect of mPEG-SH on Ag nanoplates, the nanoplates were reacted with various amounts of mPEG-SH, washed, and then resuspended in DPBS. The extinction spectrum of the nanoplates was then monitored over time. Briefly, the growth solution was removed from a B3 after synthesis using a 50 kDa MWCO Millipore centrifugal filter spun at 1500 rcf for 5 min at 20°C. The B3 nanoplates were then resuspended in 3 ml of DIUF water. To one batch of nanoplates, 445 µl of 5 mM mPEG-SH was added, and to the other batch, 445 µl of 0.083 mM mPEG-SH was added (representing a 30-fold excess of mPEG-SH surface area coverage on the first nanoplate sample, and only 50% surface area coverage on the second sample). Each sample was allowed to react at room temperature, in the dark, while shaking for 15 min. Excess mPEG-SH was then removed from each sample using a 50 kDa MWCO Millipore centrifugal filter spun at 1500 rcf for 5 min at 20°C. Each sample was resuspended to an optical density of ~1 (using a 1 cm path length) in Dulbecco's Phosphate Buffered Saline (DPBS). The extinction spectrum of the nanoplates was captured at various times over the next 60 days. Each sample was stored in a sealed plastic cuvette at 4°C for the duration of the experiment.

In vitro cell labeling with antibody and poly(ethylene glycol) conjugated Ag nanoplates

The human pancreatic cancer cell line, MPanc96, was mixed in media with two types of Ag nanoplates: nanoplates conjugated to a-EGFR and PEG, and nanoplates conjugated only to PEG. Briefly, approximately 300,000 MPanc96 cells were suspended in 500 µl of media in two separate sterile 2 ml tubes. To each respective tube, 50 µl of the as prepared a-EGFR and PEG conjugated nanoplates, and the PEG conjugated nanoplates were mixed. The tubes were shaken every 30 min over a 4 hr period while in the incubator. After 4 hours, the cells were spun down in their tubes at 125 rcf for 5 min at 4°C. They were resuspended in 2 wt% formalin in DPBS, allowed to sit for 20 min, and then washed 2× with the 2 wt% formalin in DPBS solution. The cells were fixed on a microscope slide using Vectashield with Dapi mounting solution and imaged in fluorescence and darkfield modes of a Leica DMI3000 B inverted microscope with a Leica DFC 290 kit and 3 mega pixel color camera.

In vitro cytotoxicity studies of Ag nanoplates

Two human pancreatic cancer cell lines, L3.6pl and MPanc96, and the non-cancerous pancreatic line, HPNE, were incubated with Ag nanoplates and tested for cell viability. Both cancer cell lines were cultured *in vitro* using Dulbecco's Modified Eagle Medium (DMEM) (with 4500 mg glucose/L, L-glutamine, NaHCO$_3$ and pyridoxine HCl) supplemented with 10% fetal bovine serum (FBS) and 1% Penicillin-Streptomycin (Pen/Strep) while maintained at 37°C and 5% CO$_2$ in a humidified incubator. For the pancreatic cancer cell lines, the DMEM and the FBS were purchased from Sigma, while the Pen/Strep was purchased from Invitrogen. The non-cancerous pancreatic cell line, HPNE, was cultured *in vitro* using Medium D that contained one volume of medium M3, three volumes of glucose-

free DMEM (with L-glutamine, phenol red, and pyridoxine HCl from Invitrogen), 5% FBS, 5.5 mM glucose, 10 ng/ml EGF (Invitrogen), and 50 μg/ml gentamycin (Sigma). Medium M3 is a proprietary formulation optimized for the growth of neuroendocrine cells (InCell Corp., San Antonio, TX, USA). For cell viability studies, cells were seeded in a 96 well plate (each well had 5,000 cells per 100 μl of media). The cells were allowed to attach and grow in the 96 well plate for 48 hr, after which the cell media was removed and replaced with 100 μl suspensions of a-EGFR- and PEG-conjugated Ag nanoplates at various concentrations representing 1 mg/ml, 0.5 mg/ml, 0.25 mg/ml, 0.125 mg/ml, 0.0625 mg/ml and 0 mg/ml of silver (at least 5 wells were seeded with each concentration). Note that the highest silver concentration at 1 mg/ml represented ~1.2×10^{12} nanoplates per ml, while the lowest silver concentration at 0.0625 mg/ml represented ~7.3×10^{10} nanoplates per ml. After 24 hr of incubation, the media was removed and replaced with fresh media containing no nanoplates. The absorbance of each well in the plate was measured at 490 nm using a Synergy HT Multimode Microplate Reader from BioTek. To perform the assay, 20 μl of a tetrazolium compound [3-(4,5-dimethylthiazol-2-yl)-5-(3-carboxymethoxyphenyl)-2-(4-sulfophenyl)-2H-tetrazolium (MTS) and an electron coupling reagent (phenazine methosulfate) PMS from the CellTiter 96® AQ$_{ueous}$ Non-Radioactive Cell Proliferation Assay (a Promega product) was added to each well. Over a period of 1 hr in the incubator, the MTS was bioreduced by cells into a formazan product that had an absorbance peak at 490 nm. Dehydrogenase enzymes found in metabolically active cells were responsible for the conversion of MTS into the soluble formazan product. Therefore, the absorbance of each well at 490 nm was directly proportional to the number of viable cells. The absorbance of each well at 490 nm taken before adding MTS was subtracted from the after MTS incubation value. Cell viability was determined by comparing the resulting absorbance of wells containing no nanoplates to wells containing nanoplates using an F test for a one-way ANOVA.

Animal models

Xenograft tumors were grown orthotopically in Nu/Nu mice to test the *in vivo* targeting and imaging capabilities of the a-EGFR conjugated nanoplates (the nanoplates were also passivated with mPEG-SH as described above). Specifically, after administering anesthesia to the mouse (avertin), surgery was performed to expose the pancreas and inject 50 μl containing 200,000 L3.6pl cells suspended in sterile DPBS. After approximately two weeks of growth, the tumor was mature and the combined USPA imaging experiment was conducted with the mouse situated on a heated electrocardiogram pad where temperature and heart rate could be monitored while the animal was under anesthesia (isoflurane). After collecting US and PA data on the tumor area in what we term "before" images, the mouse was injected (*via* the tail vein) with ~10^{12} a-EGFR conjugated, PEG passivated Ag nanoplates in 200 μl of PBS (LSPR peak of 800 nm). US and PA data was then collected every hour for the first 6 hr after injection. All procedures were conducted in accordance with the protocols approved by the Institutional Animal Care and Use Committee at The University of Texas at Austin.

Combined ultrasound and photoacoustic (USPA) imaging system

To perform *in vivo* imaging experiments, a custom designed combined USPA imaging system was used as previously described.[6, 65–67] The setup for the combined USPA imaging system consisted of pulsed light in the range of wavelengths between 740 nm and 940 nm generated by an optical parametric oscillator (OPO) Spectraphysics laser system operating at 10 Hz with a 5–7 ns pulse duration. The pulsed light illuminated the side of the mouse, encompassing the tumor region, at fluences ranging from 10 mJ/cm^2 to 15 mJ/cm^2. An array transducer (9 MHz center frequency, 14 mm wide, 128 element linear array) collected the ultrasound data from above. To collect radiofrequency (RF) data, the transducer was

interfaced with a Cortex ultrasound imaging engine (Winprobe Corp) capable of RF data acquisition for spatially co-registered US and PA RF signals. To form images, the RF data was beamformed using a delay-and-sum approach. The PA spectrum measured at each pixel was compared to known endogenous absorption spectra in the literature[68] and the extinction spectrum of Ag nanoplates. Each component was classified using a least squared errors estimation method[67, 69] to form a spectroscopic PA image. The US images (displayed using dB scale) and fluence-compensated spectroscopic PA images (displayed using linear scale) were plotted. Three-dimensional renderings were obtained by stacking 21 two-dimensional slices spaced 400 μm apart.

Supplementary Material

Refer to Web version on PubMed Central for supplementary material.

Acknowledgments

REFERENCES

1. Weissleder R. Molecular Imaging in Cancer. Science. 2006; 312:1168–1171. [PubMed: 16728630]

2. Xu M, Wang LV. Photoacoustic Imaging in Biomedicine. Rev. Sci. Instrum. 2006; 77:041101.

3. Emelianov SY, Aglyamov SR, Karpiouk AB, Mallidi S, Park S, Sethuraman S, Shah S, Smalling RW, Rubin JM, Scott WG. Synergy and Applications of Ultrasound, Elasticity, and Photoacoustic Imaging. Proceedings of the IEEE Ultrasonics Symposium. 2006:405–415.

4. Kolkman RG, Brands PJ, Steenbergen W, van Leeuwen TG. Real-Time in Vivo Photoacoustic and Ultrasound Imaging. J Biomed Opt. 2008; 13:050510. [PubMed: 19021380]

5. Kruger RA, Liu P, Fang YR, Appledorn CR. Photoacoustic Ultrasound (Paus) Reconstruction Tomography. Med. Phys. 1995; 22:1605–1609. [PubMed: 8551984]

6. Homan K, Kim S, Chen YS, Wang B, Mallidi S, Emelianov S. Prospects of Molecular Photoacoustic Imaging at 1064 Nm Wavelength. Opt Lett. 2010; 35:2663–2665. [PubMed: 20680092]

7. Jose J, Manohar S, Kolkman RG, Steenbergen W, van Leeuwen TG. Imaging of Tumor Vasculature Using Twente Photoacoustic Systems. J Biophotonics. 2009; 2:701–717. [PubMed: 19718681]

8. Kolkman RG, Mulder MJ, Glade CP, Steenbergen W, van Leeuwen TG. Photoacoustic Imaging of Port-Wine Stains. Lasers Surg. Med. 2008; 40:178–182. [PubMed: 18366079]

9. Ku G, Wang X, Xie X, Stoica G, Wang LV. Imaging of Tumor Angiogenesis in Rat Brains in Vivo by Photoacoustic Tomography. Appl Opt. 2005; 44:770–775. [PubMed: 15751858]

10. Staley J, Grogan P, Samadi AK, Cui H, Cohen MS, Yang X. Growth of Melanoma Brain Tumors Monitored by Photoacoustic Microscopy. J Biomed Opt. 2010; 15:040510. [PubMed: 20799777]

11. Zhang HF, Maslov K, Stoica G, Wang LV. Functional Photoacoustic Microscopy for High-Resolution and Noninvasive in Vivo Imaging. Nat. Biotechnol. 2006; 24:848–851. [PubMed: 16823374]

12. Yao J, Wang LV. Photoacoustic Tomography: Fundamentals, Advances and Prospects. Contrast Media Mol Imaging. 2011; 6:332–345. [PubMed: 22025335]

13. Hockel M, Vaupel P. Tumor Hypoxia: Definitions and Current Clinical, Biologic, and Molecular Aspects. J. Natl. Cancer Inst. 2001; 93:266–276. [PubMed: 11181773]

14. Mallidi S, Luke GP, Emelianov S. Photoacoustic Imaging in Cancer Detection, Diagnosis, and Treatment Guidance. Trends Biotechnol. 2011; 29:213–221. [PubMed: 21324541]

15. Homan K, Gomez S, Gensler H, Shah J, Brannon-Peppas L, Emelianov S. Design and Development of Multifunctional Contrast Agents for Photoacoustic Imaging. Reporters, Markers, Dyes, Nanoparticles, and Molecular Probes for Biomedical Applications: Proceedings of the SPIE. 2009; 7190:71900I–71900I.

16. Joshi, P.; Chen, Y-S.; Kim, S.; Shah, J.; Emelianov, S. Molecular Therapeutic Agents for Noninvasive Photoacoustic Image-Guided Photothermal Therapy. 31st Annual International IEEE The Engineering in Medicine and Biology Conference (EMBC) Proceedings; 2009. p. 1158

17. Kim C, Cho EC, Chen J, Song KH, Au L, Favazza C, Zhang Q, Cobley CM, Gao F, Xia Y, et al. In Vivo Molecular Photoacoustic Tomography of Melanomas Targeted by Bioconjugated Gold Nanocages. ACS Nano. 2010; 4:4559–4564. [PubMed: 20731439]

18. Kim JW, Galanzha EI, Shashkov EV, Moon HM, Zharov VP. Golden Carbon Nanotubes as Multimodal Photoacoustic and Photothermal High-Contrast Molecular Agents. Nat Nanotechnol. 2009; 4:688–694. [PubMed: 19809462]

19. Li PC, Wei CW, Liao CK, Chen CD, Pao KC, Wang CR, Wu YN, Shieh DB. Photoacoustic Imaging of Multiple Targets Using Gold Nanorods. IEEE Trans Ultrason Ferroelectr Freq Control. 2007; 54:1642–1647. [PubMed: 17703668]

20. Wilson K, Homan K, Emelianov S. Synthesis of a Dual Contrast Agent for Ultrasound and Photoacoustic Imaging. Reporters, Markers, Dyes, Nanoparticles, and Molecular Probes for Biomedical Applications II Proc. SPIE. 2010; 7576:75760M.

21. Luke GP, Yeager D, Emelianov SY. Biomedical Applications of Photoacoustic Imaging with Exogenous Contrast Agents. Ann. Biomed. Eng. 2011

22. Homan, K.; Mallidi, S.; Cooley, E.; Emelianov, S. Combined Photoacoustic and Ultrasound Imaging of Metal Nanoparticles in Vivo. In: Goins, B.; Phillips, W., editors. Nanoimaging. Vol. Vol. 3. Pan Stanford Publishing; Singapore: 2011.

23. Oraevsky, AA. Gold and Silver Nanoparticles as Contrast Agents for Optoacoustic Imaging. In: Wang, LV., editor. Photoacoustic Imaging and Spectroscopy. Taylor and Francis Group; New York: 2009.

24. Agarwal A, Huang SW, O'Donnell M, Day KC, Day M, Kotov N, Ashkenazi S. Targeted Gold Nanorod Contrast Agent for Prostate Cancer Detection by Photoacoustic Imaging. J. Appl. Phys. 2007; 102:064701.

25. Chen YS, Frey W, Kim S, Kruizinga P, Homan K, Emelianov S. Silica-Coated Gold Nanorods as Photoacoustic Signal Nanoamplifiers. Nano Lett. 2011; 11:348–354. [PubMed: 21244082]

26. Pan D, Pramanik M, Senpan A, Ghosh S, Wickline SA, Wang LV, Lanza GM. Near Infrared Photoacoustic Detection of Sentinel Lymph Nodes with Gold Nanobeacons. Biomaterials. 2010; 31:4088–4093. [PubMed: 20172607]

27. Skrabalak SE, Chen J, Sun Y, Lu X, Au L, Cobley CM, Xia Y. Gold Nanocages: Synthesis, Properties, and Applications. Acc Chem Res. 2008; 41:1587–1595. [PubMed: 18570442]

28. Pan D, Pramanik M, Wickline SA, Wang LV, Lanza GM. Recent Advances in Colloidal Gold Nanobeacons for Molecular Photoacoustic Imaging. Contrast Media Mol Imaging. 2011; 6:378–388. [PubMed: 22025338]

29. Biju V, Itoh T, Anas A, Sujith A, Ishikawa M. Semiconductor Quantum Dots and Metal Nanoparticles: Syntheses, Optical Properties, and Biological Applications. Anal Bioanal Chem. 2008; 391:2469–2495. [PubMed: 18548237]

30. Hao E, Schatz GC, Hupp JT. Synthesis and Optical Properties of Anisotropic Metal Nanoparticles. J Fluoresc. 2004; 14:331–341. [PubMed: 15617376]

31. Jiang XC, Chen CY, Chen WM, Yu AB. Role of Citric Acid in the Formation of Silver Nanoplates through a Synergistic Reduction Approach. Langmuir. 2009

32. Martínez-Castañón G, Niño-Martínez N, Loyola-Rodríguez J, Patiño-Marín N, Martínez-Mendoza J, Ruiz F. Synthesis of Silver Particles with Different Sizes and Morphologies. Mater. Lett. 2009

33. Metraux C, Mirkin C. Rapid Thermal Synthesis of Silver Nanoprisms with Chemically Tailorable Thickness. Adv. Mater. 2005; 17:412–415.

34. Murphy CJ, Sau TK, Gole AM, Orendorff CJ, Gao J, Gou L, Hunyadi SE, Li T. Anisotropic Metal Nanoparticles: Synthesis, Assembly, and Optical Applications. J Phys Chem B. 2005; 109:13857–13870. [PubMed: 16852739]

35. Sharma VK, Yngard RA, Lin Y. Silver Nanoparticles: Green Synthesis and Their Antimicrobial Activities. Adv. Colloid Interface Sci. 2009; 145:83–96. [PubMed: 18945421]

36. Suber L, Sondi I, Matijevic E, Goia DV. Preparation and the Mechanisms of Formation of Silver Particles of Different Morphologies in Homogeneous Solutions. J. Colloid Interface Sci. 2005; 288:489–495. [PubMed: 15927616]

37. Sun Y, Xia Y. Shape-Controlled Synthesis of Gold and Silver Nanoparticles. Science. 2002; 298:2176–2179. [PubMed: 12481134]

38. Wiley B, Sun Y, Xia Y. Synthesis of Silver Nanostructures with Controlled Shapes and Properties. Acc Chem Res. 2007; 40:1067–1076. [PubMed: 17616165]

39. Xue C, Metraux GS, Millstone JE, Mirkin CA. Mechanistic Study of Photomediated Triangular Silver Nanoprism Growth. J. Am. Chem. Soc. 2008; 130:8337–8344. [PubMed: 18533653]

40. Xue C, Mirkin CA. Ph-Switchable Silver Nanoprism Growth Pathways. Angew. Chem. Int. Ed. Engl. 2007; 46:2036–2038. [PubMed: 17295376]

41. Zou X, Ying E, Chen H, Dong S. An Approach for Synthesizing Nanometer-to Micrometer-Sized Silver Nanoplates. Colloids Surf. Physicochem. Eng. Aspects. 2007; 303:226–234.

42. Sakamoto M, Fujistuka M, Majima T. Light as a Construction Tool of Metal Nanoparticles: Synthesis and Mechanism. Journal of Photochemistry & Photobiology, C: Photochemistry Reviews. 2009; 10:33–56.

43. Ramanathan R, O'Mullane AP, Parikh RY, Smooker PM, Bhargava SK, Bansal V. Bacterial Kinetics-Controlled Shape-Directed Biosynthesis of Silver Nanoplates Using Morganella Psychrotolerans. Langmuir. 2011; 27:714–719. [PubMed: 21142094]

44. Xie J, Lee JY, Wang DI, Ting YP. Silver Nanoplates: From Biological to Biomimetic Synthesis. ACS Nano. 2007; 1:429–439. [PubMed: 19206664]

45. Skrabalak SE, Au L, Li X, Xia Y. Facile Synthesis of Ag Nanocubes and Au Nanocages. Nat Protoc. 2007; 2:2182–2190. [PubMed: 17853874]

46. Xia Y, Xiong Y, Lim B, Skrabalak SE. Shape-Controlled Synthesis of Metal Nanocrystals: Simple Chemistry Meets Complex Physics? Angew. Chem. Int. Ed. Engl. 2009; 48:60–103. [PubMed: 19053095]

47. Sherry LJ, Jin R, Mirkin CA, Schatz GC, Van Duyne RP. Localized Surface Plasmon Resonance Spectroscopy of Single Silver Triangular Nanoprisms. Nano Lett. 2006; 6:2060–2065. [PubMed: 16968025]

48. Kelly K, Coronado E, Zhao L, Schatz G. The Optical Properties of Metal Nanoparticles: The Influence of Size, Shape, and Dielectric Environment. Journal of Physical Chemistry B-Condensed Phase. 2003; 107:668–677.

49. Owens DE 3rd, Peppas NA. Opsonization, Biodistribution, and Pharmacokinetics of Polymeric Nanoparticles. Int. J. Pharm. 2006; 307:93–102. [PubMed: 16303268]

50. Bergen JM, von Recum HA, Goodman TT, Massey AP, Pun SH. Gold Nanoparticles as a Versatile Platform for Optimizing Physicochemical Parameters for Targeted Drug Delivery. Macromol Biosci. 2006; 6:506–516. [PubMed: 16921538]

51. Levin CS, Bishnoi SW, Grady NK, Halas NJ. Determining the Conformation of Thiolated Poly(Ethylene Glycol) on Au Nanoshells by Surface-Enhanced Raman Scattering Spectroscopic Assay. Anal. Chem. 2006; 78:3277–3281. [PubMed: 16689527]

52. Diagaradjane P, Orenstein-Cardona JM, Colon-Casasnovas NE, Deorukhkar A, Shentu S, Kuno N, Schwartz DL, Gelovani JG, Krishnan S. Imaging Epidermal Growth Factor Receptor Expression in Vivo: Pharmacokinetic and Biodistribution Characterization of a Bioconjugated Quantum Dot Nanoprobe. Clin. Cancer Res. 2008; 14:731–741. [PubMed: 18245533]

53. Rosenthal EL, Kulbersh BD, King T, Chaudhuri TR, Zinn KR. Use of Fluorescent Labeled Anti-Epidermal Growth Factor Receptor Antibody to Image Head and Neck Squamous Cell Carcinoma Xenografts. Mol Cancer Ther. 2007; 6:1230–1238. [PubMed: 17431103]

54. Sokolov K, Follen M, Aaron J, Pavlova I, Malpica A, Lotan R, Richards-Kortum R. Real-Time Vital Optical Imaging of Precancer Using Anti-Epidermal Growth Factor Receptor Antibodies Conjugated to Gold Nanoparticles. Cancer Res. 2003; 63:1999–2004. [PubMed: 12727808]

55. Kumar S, Aaron J, Sokolov K. Directional Conjugation of Antibodies to Nanoparticles for Synthesis of Multiplexed Optical Contrast Agents with Both Delivery and Targeting Moieties. Nat Protoc. 2008; 3:314–320. [PubMed: 18274533]

56. Aaron J, Travis K, Harrison N, Sokolov K. Dynamic Imaging of Molecular Assemblies in Live Cells Based on Nanoparticle Plasmon Resonance Coupling. Nano Lett. 2009; 9:3612–3618. [PubMed: 19645464]

57. Bhattacharyya S, Bhattacharya R, Curley S, McNiven MA, Mukherjee P. Nanoconjugation Modulates the Trafficking and Mechanism of Antibody Induced Receptor Endocytosis. Proc. Natl. Acad. Sci. U. S. A. 2010; 107:14541–14546. [PubMed: 20679244]

58. El-Sayed IH, Huang X, El-Sayed MA. Surface Plasmon Resonance Scattering and Absorption of Anti-Egfr Antibody Conjugated Gold Nanoparticles in Cancer Diagnostics: Applications in Oral Cancer. Nano Lett. 2005; 5:829–834. [PubMed: 15884879]

59. AshaRani PV, Low Kah Mun G, Hande MP, Valiyaveettil S. Cytotoxicity and Genotoxicity of Silver Nanoparticles in Human Cells. ACS Nano. 2009; 3:279–290. [PubMed: 19236062]

60. Asharani PV, Hande MP, Valiyaveettil S. Anti-Proliferative Activity of Silver Nanoparticles. BMC Cell Biol. 2009; 10:65. [PubMed: 19761582]

61. Johnston HJ, Hutchison G, Christensen FM, Peters S, Hankin S, Stone V. A Review of the in Vivo and in Vitro Toxicity of Silver and Gold Particulates: Particle Attributes and Biological Mechanisms Responsible for the Observed Toxicity. Crit. Rev. Toxicol. 2010; 40:328–346. [PubMed: 20128631]

62. Li ML, Wang JC, Schwartz JA, Gill-Sharp KL, Stoica G, Wang LV. In-Vivo Photoacoustic Microscopy of Nanoshell Extravasation from Solid Tumor Vasculature. J Biomed Opt. 2009; 14:010507. [PubMed: 19256687]

63. Brigger I, Dubernet C, Couvreur P. Nanoparticles in Cancer Therapy and Diagnosis. Adv Drug Deliv Rev. 2002; 54:631–651. [PubMed: 12204596]

64. Rasband, WS. ImageJ. http://imagej.nih.gov/ij/

65. Homan, K.; Shah, J.; Gomez, S.; Gensler, H.; Karpiouk, A.; Brannon-Peppas, L.; Emelianov, S. Combined Ultrasound and Photoacoustic Imaging of Pancreatic Cancer Using Nanocage Contrast Agents. SPIE Photonics West; San Jose, CA, USA: 2009. p. 71771MProceedings of the SPIE: San Jose, CA, USA

66. Homan K, Shah J, Gomez S, Gensler H, Karpiouk A, Brannon-Peppas L, Emelianov S. Silver Nanosystems for Photoacoustic Imaging and Image-Guided Therapy. Journal of Biomedical Optics. 2010; 15:021316. [PubMed: 20459238]

67. Kim S, Chen YS, Luke GP, Emelianov SY. In Vivo Three-Dimensional Spectroscopic Photoacoustic Imaging for Monitoring Nanoparticle Delivery. Biomedical Optics Express. 2011; 2:2540–2550. [PubMed: 21991546]

68. Prahl, SA. Optical Property Spectra Compiled by Scott Prahl. http://omlc.ogi.edu/spectra/

69. Li ML, Oh JT, Xie X, Ku G, Wang W, Li C, Lungu G, Stoica G, Wang L. Simultaneous Molecular and Hypoxia Imaging of Brain Tumors in Vivo Using Spectroscopic Photoacoustic Tomography. Proceedings of the IEEE. 2008; 96:481–489.
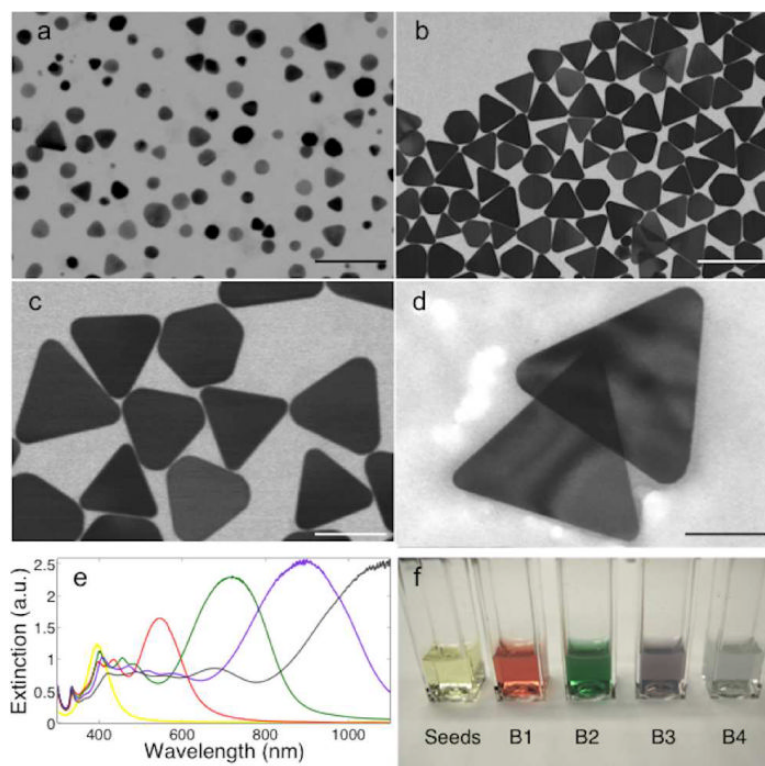
Figure 1.
Silver nanoplates directly after step-wise growth adding edge length from B1 to B4 (a–d) with their corresponding extinction spectra (e) and color change in solution (f). Scale bars are 100 nm.
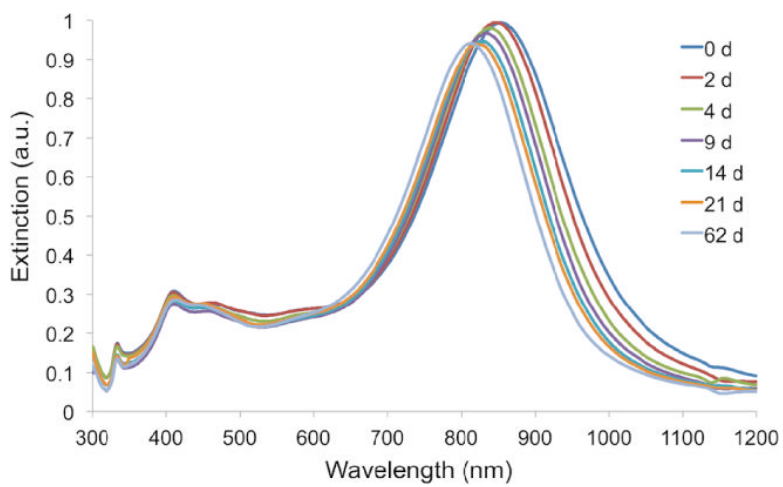
Figure 2.
Demonstration of the biostability of PEGylated Ag nanoplates suspended in saline solution over a period of 62 days.
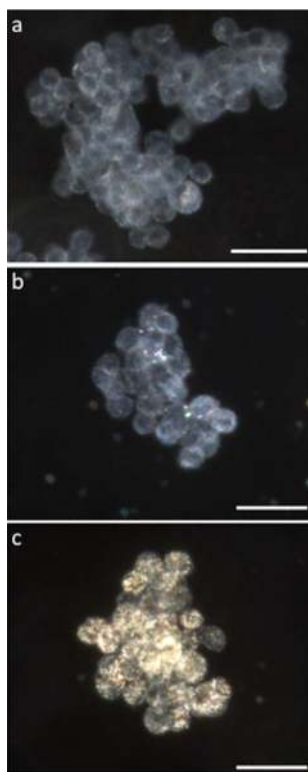
Figure 3.
Darkfield microscopy of pancreatic cancer cells after incubation with no nanoplates (a), PEGylated nanoplates (b), and a-EGFR conjugated nanoplates (c). All scale bars are 20 µm.
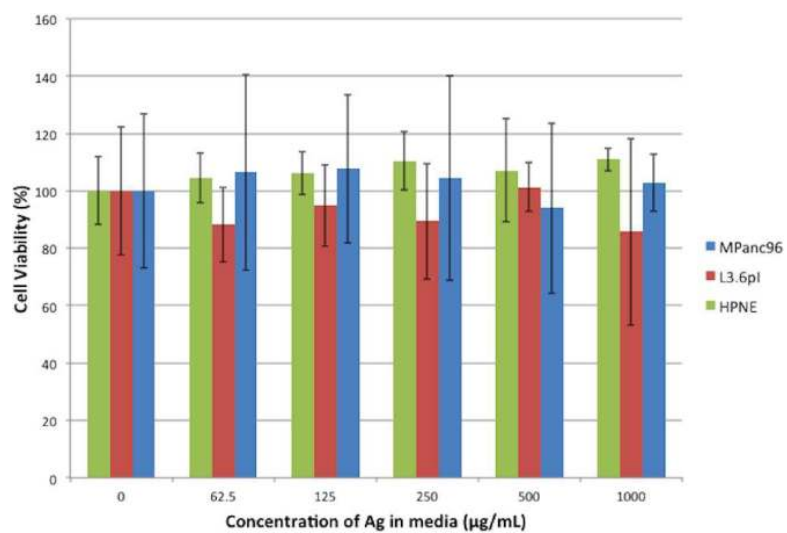
Figure 4.
Results of the MTS assay for cell viability on three cell lines after incubation for 24 hr with a-EGFR conjugated Ag nanoplates at various concentrations.
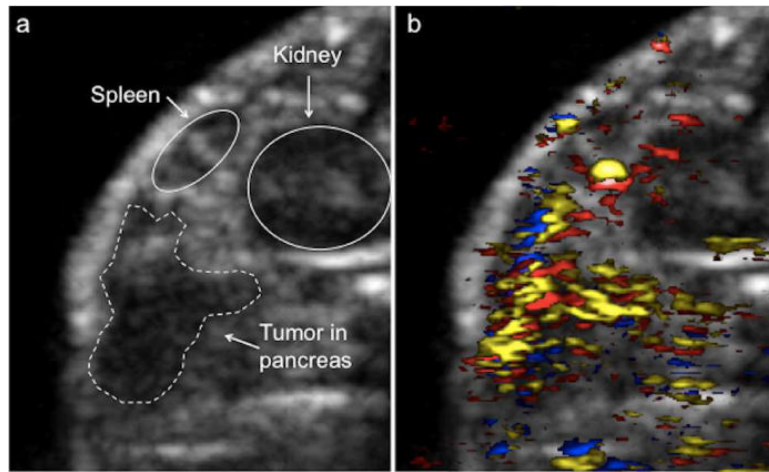
Figure 5.
2-D cross sections of an orthotopic pancreatic tumor in a nude mouse model. US image (a) shows the anatomical features, while the USPA image (b) shows molecular accumulation of a-EGFR conjugated nanoplates (yellow), oxygenated blood (red), and deoxygenated blood (blue). Image dimensions are 14.5 mm by 11.8 mm.
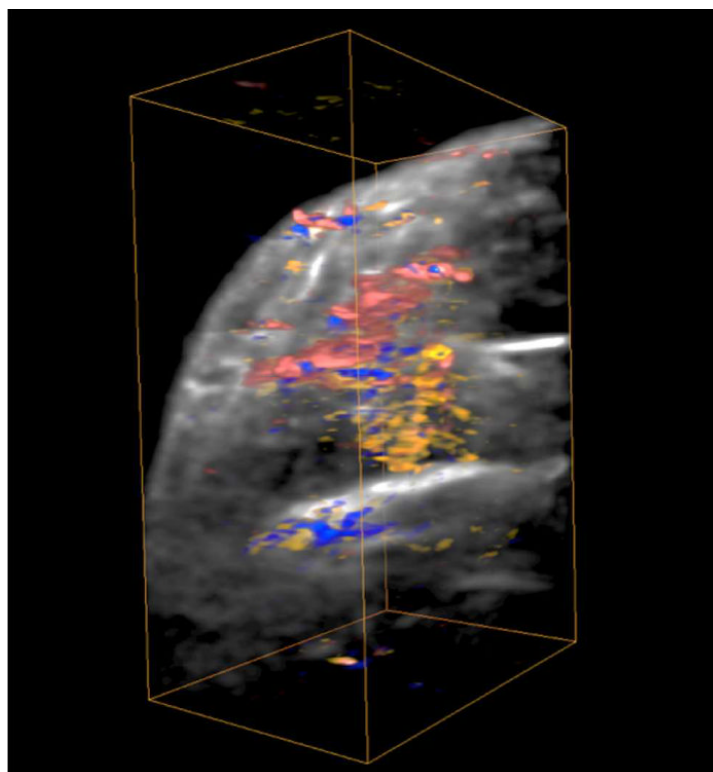
Figure 6.
Reconstructed 3-D USPA image of an orthotopic pancreatic tumor in a mouse model. The PA visualization of accumulated a-EGFR-conjugated nanoplates (yellow), oxygenated blood (red), and deoxygenated blood (blue) is shown overlaid on the US image of the mouse anatomy. Image dimensions are 8 mm by 17.5 mm by 11.8 mm.
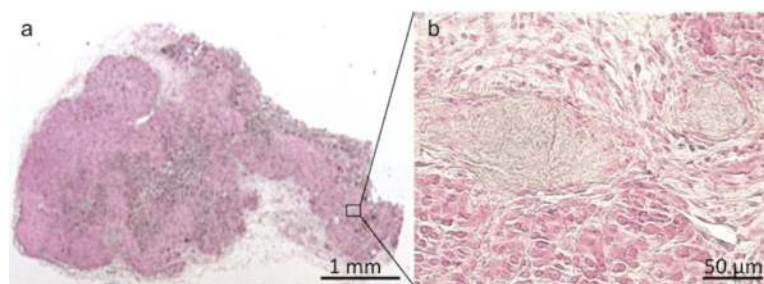
Figure 7.
Histological cross-section of the orthotopic pancreatic tumor imaged using USPA imaging. The section is stained with nuclear fast red (pink areas) and silver stain (dark areas in the slice that indicate the presence of Ag nanoplates). The distribution of the nanoplates is heterogeneous and correlates with the distribution of nanoplates displayed in USPA imaging.

Table 1

Size chart of Ag nanoplate edge length and thickness for each growth step along with the LSPR peak for each batch.

	Nanoplate Edge Length (nm)	Nanoplate Thickness (nm)	LSPR peak (nm)
B1	25.3 ± 5.5	10.4 ± 1.6	550
B2	60.9 ± 10.1	12.5 ± 1.9	720
B3	128.0 ± 25.9	18.0 ± 2.7	900
B4	218.6 ± 35.6	25.6 ± 6.6	1080